

Development of surrogate models of clamp configuration for optical glass lens centering through finite element analysis and machine learning

Kai Hung Yu (✉ s109033584@m109.nthu.edu.tw)

National Tsing Hua University

Shiau-Cheng Shiu

Chun-Wei Liu

Research Article

Keywords: Centering process, Surrogate model, Finite element analysis, Machine learning

Posted Date: April 11th, 2022

DOI: <https://doi.org/10.21203/rs.3.rs-1514251/v1>

License:  This work is licensed under a Creative Commons Attribution 4.0 International License.

[Read Full License](#)

Development of surrogate models of clamp configuration for optical glass lens centering through finite element analysis and machine learning

Kai-Hung Yu^{1,a}, Shiau-Cheng Shiu^{1,b}, Chun-Wei Liu^{1,c}

¹National Tsing Hua University, Power Mechanical Engineering, Section 2, Guangfu Road, Hsinchu 300044, Taiwan.

^as109033584@m109.nthu.edu.tw, ^bs109033802@m109.nthu.edu.tw, ^cweilu@pme.nthu.edu.tw

Abstract

In this study, the clamping stress and force involved in the centering of optical glass lens were evaluated and quantified. On the basis of the key design parameters of the examined clamps, the finite element method was applied to measure clamping stress under various parameter combinations. Support vector regression, Gaussian process regression, and adaptive neuro fuzzy inference system algorithm of surrogate models were established using the results obtained through finite element simulation. These surrogate models, which can predict clamping stress on the basis of key parameters, can reduce the time required to perform finite element analysis while providing references for optimizing clamp configuration.

Keywords : Centering process, Surrogate model, Finite element analysis, Machine learning

1. Introduction

An optical axis is defined as the line that connects the centers of the curvature of the curved surfaces on both sides of a lens. If the optical axis deviates from the lens' geometric center axis, the imaging position of the lens will be affected and cause aberration. Centering is a key procedure in optical glass lens manufacturing because it is required to minimize the aforementioned phenomenon [1-3]. During centering, a lens is secured by a pair of bell-shaped clamps that come into contact with both of the polished surfaces of the lens. The forces between the clamps and the lens are radially balanced. Under this condition, the optical axis coincides with the geometric center line. The lens is then grounded by a grinding wheel, such that its shape becomes perfectly symmetrical with respect to the optical axis. To prevent lens clamps from scratching the polished surfaces of lens, they must be made from soft materials. Consequently, lens clamps are prone to deforming under clamping stress, which causes the central axis of a lens to become offset. With unstable clamping, a lens can be easily pushed and decentered by a grinding wheel feed. Therefore, effective methods for evaluating and analyzing clamping stress are required for the centering process.

The finite element method (FEM) is widely used to solve engineering problems, including the evaluation of stress distribution [4] and simulation of mechanical behavior [5, 6]. FEM-derived results can also be used to conduct pre-machining assessments [7, 8] and support parameter optimization [9, 10]. However, to obtain accurate simulation results, precise engineering modeling and meshing are required. Simulating and analyzing a complex finite element model are usually tasks that require substantial time and computational resources [11, 12]. Surrogate models are often applied as substitutes of complex computational models in engineering design; they are established by using simple computational models

to simulate actual situations. Through complex finite element models, simulation results can be predicted by building a surrogate model with a learning algorithm. For example, António and Rasheed proposed a surrogate model by simulating the results of full-field displacement measurements using the FEM and training an artificial neural network (ANN) using the obtained simulation results to simplify the complex operation of the FEM [13]. Tapia et al. built a surrogate model by applying Gaussian processes regression (GPR) to predict the melt pool depth of the laser powder bed fusion process [14]. Numerous methods have been applied in other studies to construct surrogate models; these methods include support vector regression (SVR) [15-18], the response surface methodology [19-21], kriging [22-25], and the adaptive neuro fuzzy inference system (ANFIS) [26].

In the present study, a measuring method that uses load cell and strain gauge was designed to quantify the clamping force between a lens and clamps. Through adjustments to the key structural designing parameters of clamps, data on the clamping stresses under various parameter combinations were obtained through FEM simulation. Three algorithms were applied to construct surrogate models, in which structural parameters were used to predict contact stress to optimize the configuration of clamps.

2. Methodology

2.1 Relationship between clamping and grinding

The lens centering mechanism is a form of cylindrical grinding (Fig 1).

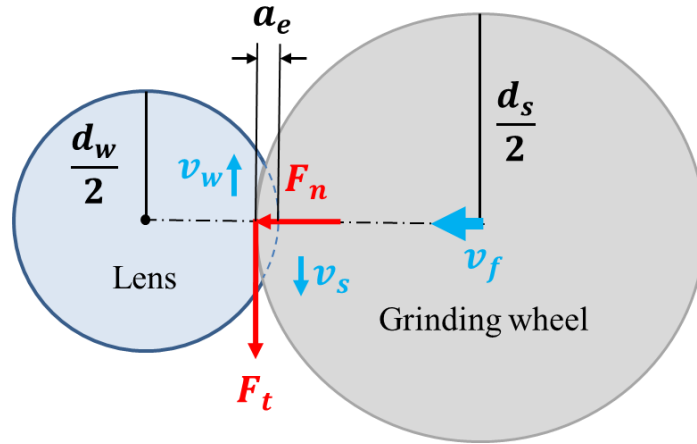


Fig 1. Cylindrical grinding.

During grinding, the stability of a lens is dependent on the frictional force f that is applied to the contact surface by the clamping force F_h ; f can be expressed using the following equation:

$$f = F_h * \mu \quad (1)$$

where μ is the friction coefficient between the lens and the clamp material. If f is less than the normal grinding force F_n or the tangential grinding force F_t induced by the grinding wheel, the lens is displaced horizontally or vertically and may also be deflected or rotated (Fig 2). Consequently, the geometric center axis of the lens is misaligned with the clamps on both sides, resulting in an optical axis error. Grinding forces can be estimated using the following equations [27]:

$$F_n = K_s * a_e \quad (2)$$

$$F_t = \frac{P}{v_s \pm v_w} \quad (3)$$

where K_s is the wear resistance constant as defined on the basis of the workpiece (i.e., the lens) and the abrasives, a_e is the effective grinding depth, P is the grinding power, v_s is the linear speed of the grinding wheel, and v_w is the horizontal speed of the workpiece.

μ_f is the grinding force ratio, that is, the ratio of the tangential and normal grinding forces; it can be obtained using the following equation:

$$\mu_f = \frac{F_t}{F_n} \quad (4)$$

Usually, μ_f is less than 0.5, which means that the normal grinding force is usually greater than the tangential grinding force [28].

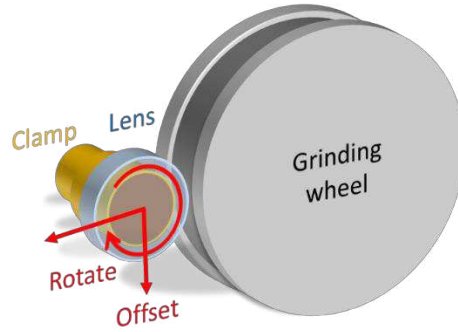


Fig 2. Lens offset.

The difficulty of centering is expressed using the coefficient Z , which is determined by the geometric shape of a lens; it is calculated using the following equation:

$$Z = \frac{\frac{D_1}{2R_1} + \frac{D_2}{2R_2}}{2} \quad (5)$$

where R is the radius of the curvature, which takes a positive number on the convex surface and a negative number on the concave surface; D_1 and D_2 are the diameters of the clamp that is in contact with R_1 and R_2 . In general, a smaller Z value indicates that the centering process is more difficult to perform. That is, the larger the contact area between a lens and a clamp, the greater the frictional force between the two items, which means that the lens is less prone to being pushed away.

2.2 Clamp design

Generally, the effective range of the polished surface of a lens is determined by its shape, and minor defects that are outside this effective range can be ignored. Therefore, a lens clamp is bell shaped, and its clamping circle must be larger than the effective range of a lens. The configuration of the contact surface between a clamp and a lens is determined by considering the morphology of the polished surface of the lens (Fig 3). If the polished surface of the lens is concave, the clamp requires an external chamfer; if the polished surface is convex, an internal chamfer is required. A clamp must apply sufficient normal force to a lens to ensure that it is not displaced by the grinding wheel and does not become deformed. Therefore, the selection of the appropriate materials for a clamp is a key step.

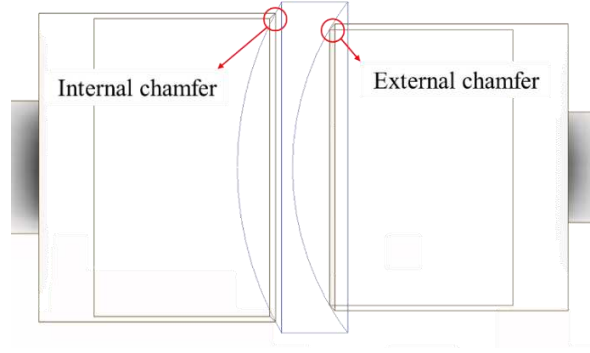


Fig 3. Contact between clamps and lens.

2.3 Optical axis error

Fig 3 shows that the area and edge difference of the contact position between the clamps and the lens affect the stress between them, which determines the deformation level of the clamps. If a clamp is deformed unevenly because of uneven force distribution or minor imperfections on its surface, the optical axis of the clamped lens deviates from the geometric center axis of the clamp on both sides, resulting in an optical axis error.

In the present study, the relationship between the peak-to-valley value of a clamp edge, the diameter of the contact area between a clamp and a lens (d), and the angle of optical axis error (θ) were mathematically analyzed (Fig 4).

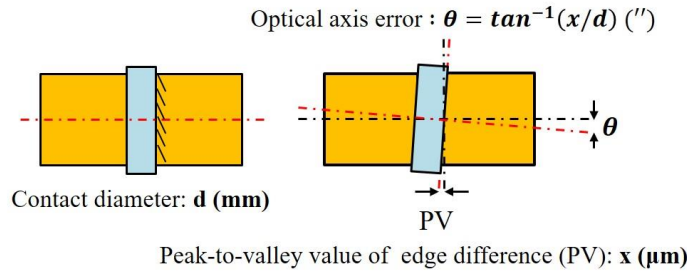


Fig 4. Relationship between edge thickness difference and optical axis error

If the contact diameters of a clamp on both sides of a clamped lens differ, their influence on the optical axis error of the lens also differ. If the lens has the three-dimensional space coordinates shown in Fig 5, then the optical axis error caused by the clamp on both sides of the lens is expressed as the angles θ_1 and θ_2 between the offset optical axis and the Z axis. After superpositioning is performed, the overall optical axis error θ_3 can be calculated using the follow equation:

$$\theta_3 = \sin^{-1}(\sqrt{(\sin\theta_1)^2 \pm 2\sin\theta_1\sin\theta_2\cos\phi + (\sin\theta_2)^2}) \quad (6)$$

where ϕ is the phase angle between θ_1 and θ_2 on the XY plane that has a positive and negative value if it is less and more than 90° , respectively.

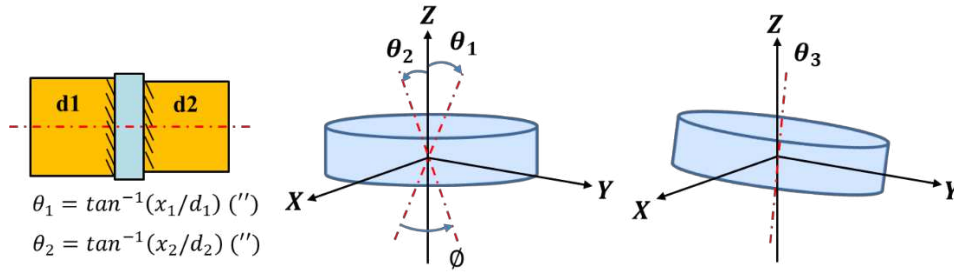


Fig 5. Superposition of the influence of a clamp (on both sides of a clamped lens) on the optical axis error of the lens.

2.4 Experiment for evaluating clamping force

2.4.1 Experimental setup

To quantify the clamping force and establish an appropriate finite element simulation load interval, a method involving the use of a load cell and strain gauges was developed for performing measurements on a centering machine. The BE-WF-502N centering machine (Shonan Optics) was used for the experiments performed in the present study. The grinding axis of the machine has three degrees of freedom on the X, Y, and A planes, and its clamping axis has two degrees of freedom on the X and A planes. The mechanism of centering is shown in Fig 6. The left end of the clamp is fixed, and the clamping handle outside the machining area drives the internal gear mechanism that allows the right end of the clamp to move along the X-plane and secure the lens.

To measure the clamping force between the clamp and a lens, a strain gauge (SHOWA N11-FA-2-120-11-VSE3) was glued to the bottom of the clamping handle, and a load cell (JIHSENSE MT-50) was clamped using the clamp. A Bridge DAQ (CHIEF SI) was used to simultaneously measure the handle strain and clamping force at a sampling rate of 200 Hz. After the relevant data were obtained, the relationship between handle strain and clamping force was further analyzed.

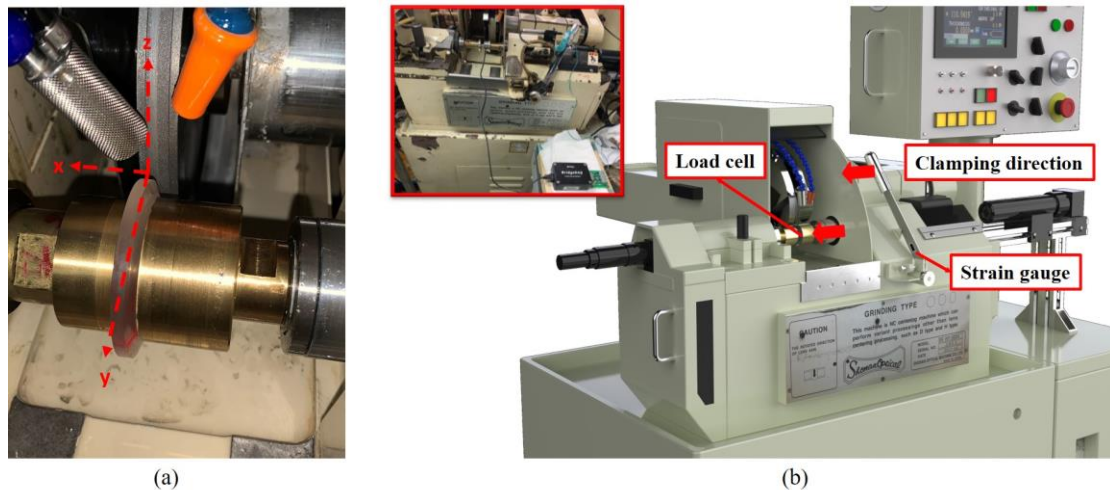


Fig 6. 502N Centering machine: (a) Processing area and (b) experimental setup.

To prevent direct contact between the load cell and the clamp, a fixture made of 6061 aluminum alloy was designed and fixed to both ends of the load cell (Fig. 7).

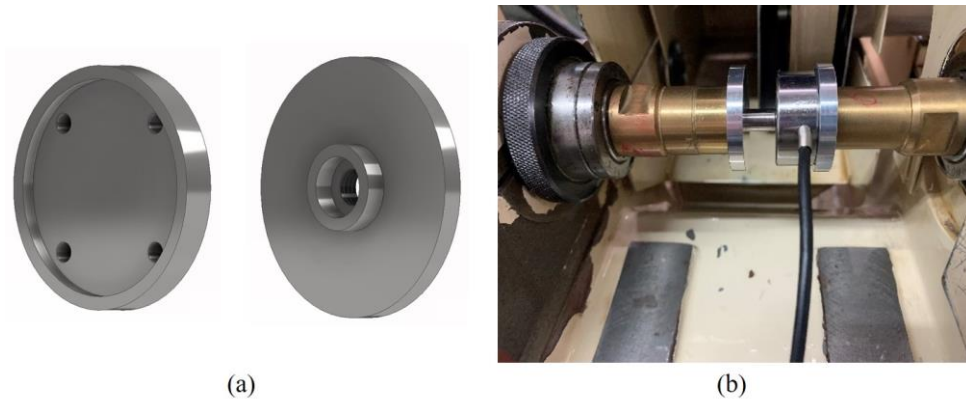


Fig 7. Load cell setup: (a) Fixture design and (b) clamping.

2.4.2 Relationship between clamping force and handle strain

For the experiments, two brass clamps, which had a diameter of 25 mm on their left sides and a diameter of 20 mm on their right sides, were used. The load cell was clamped in the manner depicted in Fig. 7(b). The strain of the handle and the load applied to the load cell were measured during the clamping process for 30 s. The obtained signal data are plotted in Fig. 8.

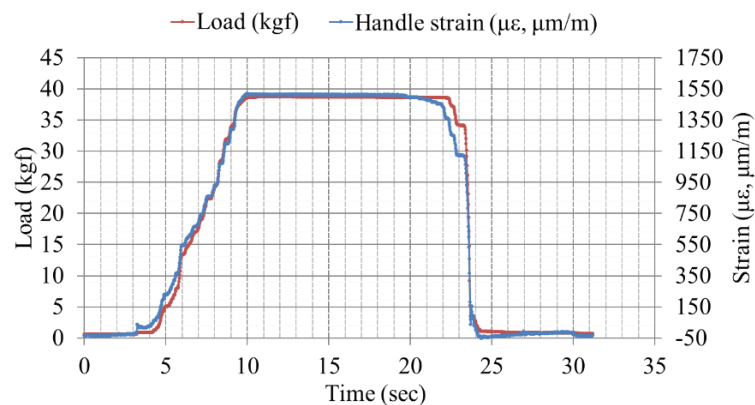


Fig 8. Strain on holding handle and load between clamp.

During the experiment, the maximum strain on the handle was 1519.16 $\mu\epsilon$, and the maximum load applied to the load cell was 38.814 kgf. Fig 9. reveals a significant linear relationship between handle strain and clamping load, and the correlation between the two was evaluated by calculating the coefficient of determination (R^2), which was determined to be 99.57%. Therefore, the handle strain could be converted into clamping force on the basis of the relationship presented in Fig. 9.

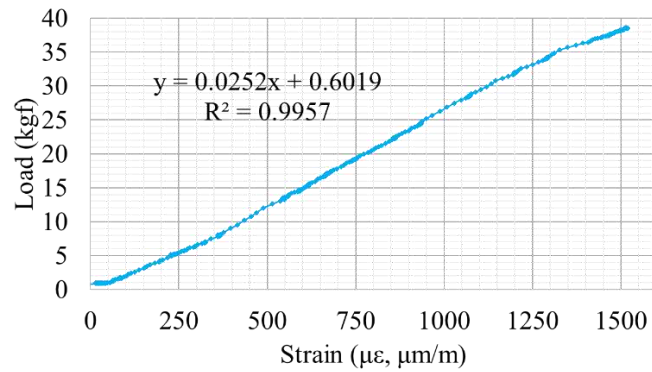


Fig 9. Relationship between load and strain

2.5 Finite element model

2.5.1 Modeling and Boundary Conditions

During the process of centering, determining whether an applied clamping force is sufficient for resisting the grinding force of the centering process is a difficult task. Furthermore, a larger force leads to greater clamp deformation, which affects the optical axis error of a lens.

A finite element analysis can be performed to obtain detailed predictions of stress, strain, and deformation. The results of a finite element analysis can be used to evaluate optical axis error, clamp deformation, and the durability of a lens centering process. Therefore, in the present study, a finite element simulation was performed to minimize clamping stress. The amount of deformation and its effect on the optical axis of a lens can be minimized by determining the minimum amount of clamping force that is required to resist grinding force.

Clamp and lens mechanical models were constructed for the finite element analysis conducted in the present study. Fig 10 shows how the contact points between the surfaces of a lens and the edges of a clamp were set in a face-to-face manner. A contact point usually experiences extremely high stress because of the limitation of a mesh. The elements on the clamp are hexagonal. For lenses, their surfaces may be concave or convex depending on their specifications. Because the curvatures of lens surfaces are variables in a simulation, a tetrahedron is the ideal type of element for modeling the shape of a lens.

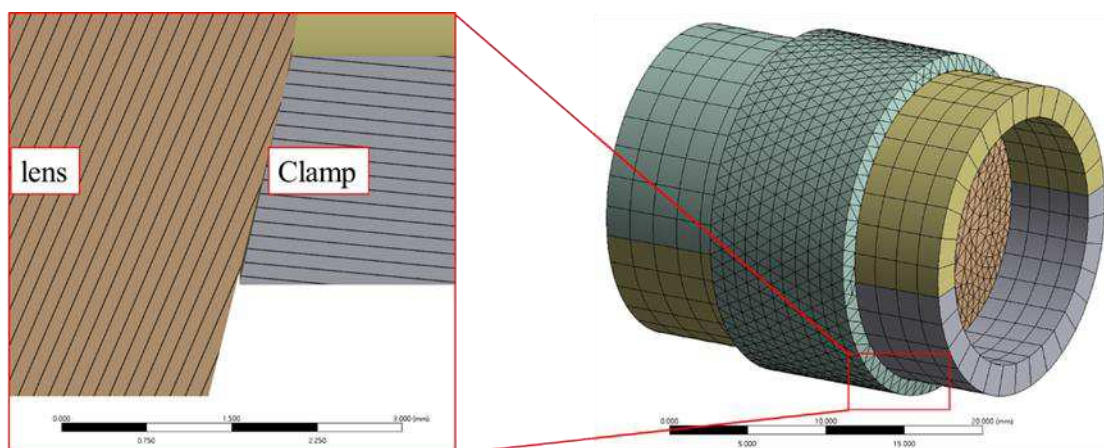


Fig 10. Contact settings and mesh configuration of clamped lens model.

The boundary conditions of the simulation performed in the present study included the clamping

force and fix support. The fix support, which fixes the geometry with a zero displacement, was positioned at the bottom of Clamp 1 (left side of the clamp in Fig 10). A clamping force was applied to Clamp 2 (right side of the clamp in Fig 10).

2.5.1 Mesh Convergence Analysis

The simulation results could be unreliable because the FEM is a numerical method that uses discrete data points. To ensure the reliability of the FEM results, an analysis of convergence was conducted. Theoretically, the result obtained from a discrete data point should be close to the actual value because the elements are highly intensive. In the analysis of convergence, element size was used as the independent variable. When element size was smaller, the number of elements increased, and the meshed elements become more intensive. The average stresses experienced by the clamps with a decreasing element size were recorded. The error of the j th iteration $e_{i,j}$ in a convergence was obtained using the following equation:

$$e_{i,j} = \frac{y_{i,j} - y_{i,j-1}}{y_{i,j-1}} \times 100\% \quad (7)$$

where $y_{i,j}$ is the simulation output y_i of the j th iteration. The outputs comprised y_1 (i.e., average surface normal stress of Clamp 1), y_2 (i.e., average surface normal stress of Clamp 2), y_3 (i.e., average surface equivalent stress [SEQV] of Clamp 1), and y_4 (i.e., average surface equivalent stress of Clamp 2).

Convergence analyses were performed for the meniscus and biconcave and biconvex lenses. Tables 1–3 and Fig. 11 reveal that the errors of the third iteration and the sixth to eighth iterations were generally less than 10% for the three types of lenses. The error value increased in the iteration that followed the third iteration. However, the sixth to eight iterations produced more reliable results because smaller element sizes were used, thus the corresponding simulation results are expected to be more accurate. Moreover, a simulation with fewer elements requires less time complete and generate results. The analyses of convergence indicated that the sixth simulation, in which an element size of 0.8 mm was used, provided the optimal balance between accuracy and simulation time.

Multiple FEM analyses were conducted, during which changes were made to clamp configuration parameters such as outer diameter, thickness (difference between the inner and outer diameters), Young’s modulus of material, and contact curvature. The simulation results were recorded, and the parameter and the corresponding maximum contact stress values were used as samples for algorithm training.

Simulation order	Element size (mm)	Iteration errors (%)			
		y1	y2	y3	y4
1	5	X	X	X	X
2	4	61.84	203.12	0.65	-0.54
3	3	2.99	2.53	0.02	3.75
4	2	33.50	32.13	3.28	3.13

5	1	27.64	29.37	-1.55	0.47
6	0.8	7.25	8.77	0.45	-3.40
7	0.6	8.17	8.10	-0.25	-2.58
8	0.5	2.18	3.90	-0.26	0.17

Table 2. Convergence analysis of bi-concave lens					
Simulation order	Element size (mm)	Iteration errors (%)			
		y1	y2	y3	y4
1	5	X	X	X	X
2	4	100.51	44.02	-2.70	0.30
3	3	-3.99	-4.12	2.01	2.07
4	2	43.54	35.46	3.35	4.90
5	1	46.96	47.08	-1.73	-1.69
6	0.8	1.18	1.46	-1.82	-1.84
7	0.6	8.48	8.36	-0.95	-0.97
8	0.5	3.49	3.34	-1.05	-1.08

Table 3. Convergence analysis of bi-convex lens					
Simulation order	Element size (mm)	Iteration errors (%)			
		y1	y2	y3	y4
1	5	X	X	X	X
2	4	5.47	3.26	-0.12	-0.11
3	3	8.32	6.35	2.35	1.29
4	2	32.56	53.54	3.43	7.61
5	1	45.29	38.76	-0.32	-2.59
6	0.8	0.66	-5.46	-1.30	-1.36
7	0.6	8.51	11.70	-0.76	-0.49
8	0.5	3.42	5.01	-1.69	-0.72

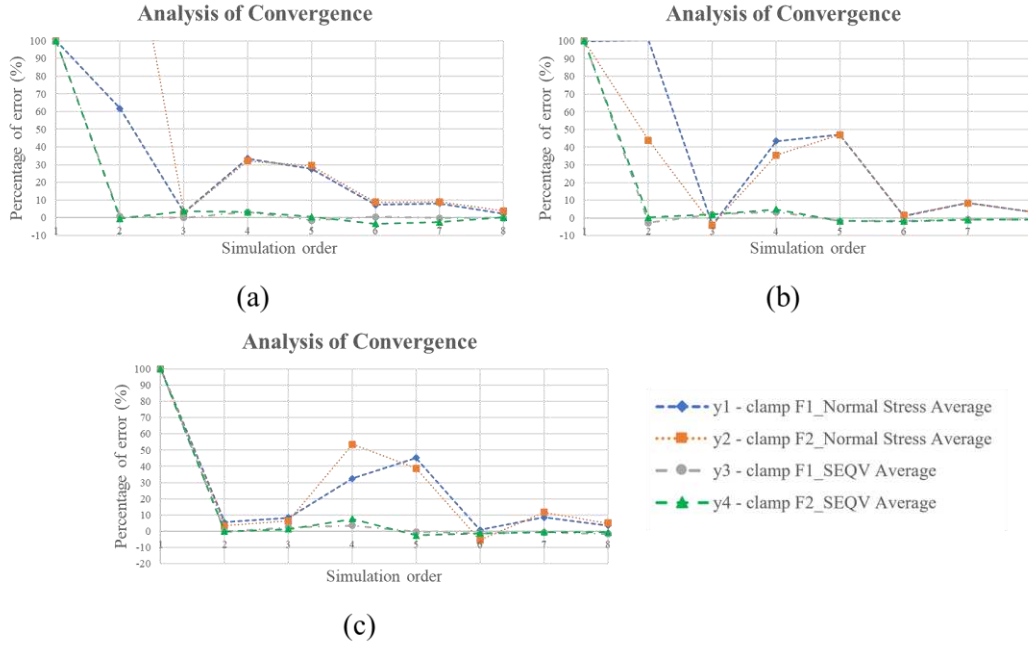


Fig 11. Convergence analysis of (a) meniscus lens, (b) bi-concave lens, and (c) bi-convex lens.

3. Surrogate model and regression analysis

3.1 SVR

SVR is a regression analysis that is based on support vector machines (SVMs). SVR and SVM algorithms are highly similar, and both are useful for classifying and predicting data with high-dimensional features. The difference between them is that an SVM model uses a hyperplane to maximize the separation between different groups of data to achieve classification, whereas an SVR model minimizes the distance of all data points to a hyperplane. In an SVR model, support vectors are used to represent data points outside a hyperplane. For the hyperplane, a ϵ value must be defined, and the boundary line is formed by $\pm\epsilon$. The distance from a support vector to a boundary is the residual ζ , and the ζ inside the hyperplane has a zero value. SVR is performed is identify the optimal ϵ value for minimizing residual error (Fig 12). With the kernel function providing various options, SVR can be applied to both linear and nonlinear classification. In the present study, a radial basis function (RBF) kernel was used for SVR modeling to accommodate the nonlinearity of prediction results.

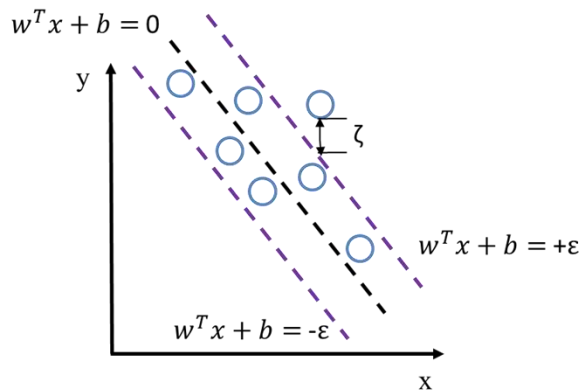


Fig 12. Support vector regression.

3.2 GPR

GPR is a nonparametric probabilistic model that is based on the Bayesian inference method; it can also be applied in both classification and regression analyses to perform accurate predictions for data with a small number of samples and features [29]. The model learns the exact values for each parameter in a function and evaluates the probability distribution of all possible values. Therefore, GPR is not limited by the form of functions. The Gaussian process can be interpreted as follows: When $x = [x_1, x_2, x_3 \dots x_n]$, and $f(x) = [f(x_1), f(x_2), f(x_3) \dots f(x_n)]$ has a multivariate Gaussian distribution, then f is a Gaussian random process that can be expressed using the following equation:

$$f(x) = N(\mu(x), k(x, x')) \quad (8)$$

where $\mu(x)$ is the mean function and $k(x, x')$ is the covariance function.

3.3 ANFIS

An ANFIS is a feed-forward ANN that is based on the Takagi–Sugeno model, which integrates fuzzy logic rules into the architecture of a neural network and thus combines the advantages of fuzzy logic networks and neural networks [30, 31]. As illustrated in Fig 12, the structure of an ANFIS can be divided into five layers in accordance with the following sequence: fuzzification layer, product layer, normalized layer, de-fuzzification layer, and output layer. In the first layer, each node is a labeled adaptive node with a membership function, and each input value (E, Z, and T) is translated into linguistic variables that represent the degree to which it conforms to a label (A, B, and C). Various types of member functions can be used, including linear, polynomial, and Gaussian functions. On the basis of the nonlinearity of the predicted clamping stress, Gaussian membership functions were applied in the present study. In the second layer, each node follows a specific fuzzy rule and generates an output that is the algebraic product of all input signals to represent the weight of the rule. The weights are then normalized in the third layer. In the fourth layer, each node is an adaptive node that provides a crisp output value on the basis of the normalized weights. The signals are then summed in the fifth layer to produce the final output value.

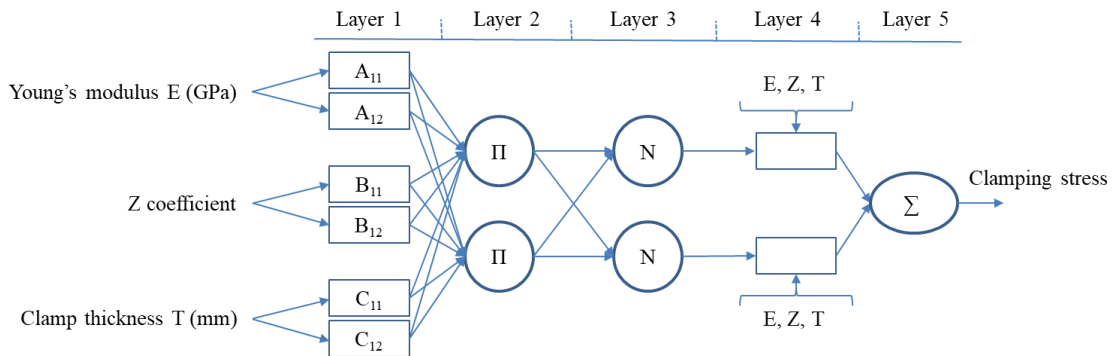


Fig 13. Structure of an adaptive neuro fuzzy inference system.

3.4 Modelling

Table 4 reveals that 590 sets of test data on three input parameters were used to train and test the aforementioned models, and the resistance-against-normal-grinding-force (MPa) data obtained from each group of parameters after the completion of a finite element simulation were used as responses in

an algorithm. In addition, 80% and 20% of the data were used for training and testing, respectively. The hyperparameters of SVR and GPR were optimized through crossvalidation, and the convergence of the model was also verified. The optimal parameters of the ANFIS used in the present study were obtained using the least squares method.

Inputs			Output
Young's modulus E (GPa)	Coefficient Z	Thickness T (mm)	Resistance against normal grinding force (MPa)
Teflon: 0.575	Between ± 1.6 Calculated by eq. (5)	Between 2 ~ 5 Common difference: 0.5	-
Aluminum: 71			
Brass: 105			
Steel: 200			

The accuracy of the model was evaluated using the coefficient of R^2 and root mean square error (RMSE), which are calculated using the residual sum of squares (RSS) and total sum of squares (TSS); the following equations are used:

$$RSS = \sum_{i=1}^n (y_i - \hat{y}_i)^2 \quad (9)$$

$$TSS = \sum_{i=1}^n (y_i - \bar{y})^2 \quad (10)$$

$$RMSE = \sqrt{\frac{1}{n} RSS} \quad (11)$$

$$R^2 = 1 - \frac{RSS}{TSS} \quad (12)$$

where y_i is the actual data point, \hat{y}_i is the predicted data point and n is the total number of data points. Generally, a smaller RMSE results in a more accurate model prediction. The closer an R^2 value is to 1, the more favorable is the the interpretability of the model. To eliminate the effect of sample size on R^2 , the adjusted R^2 is calculated using the following equation:

$$Adjusted R^2 = 1 - \frac{(1-R^2)(n-1)}{n-p-1} \quad (13)$$

where n is the sample size, and p is the number of features.

4. Results and discussion

Fig. 14 compares the results of the FEM simulation and the prediction results obtained using the SVR, GPR, and ANFIS algorithms.

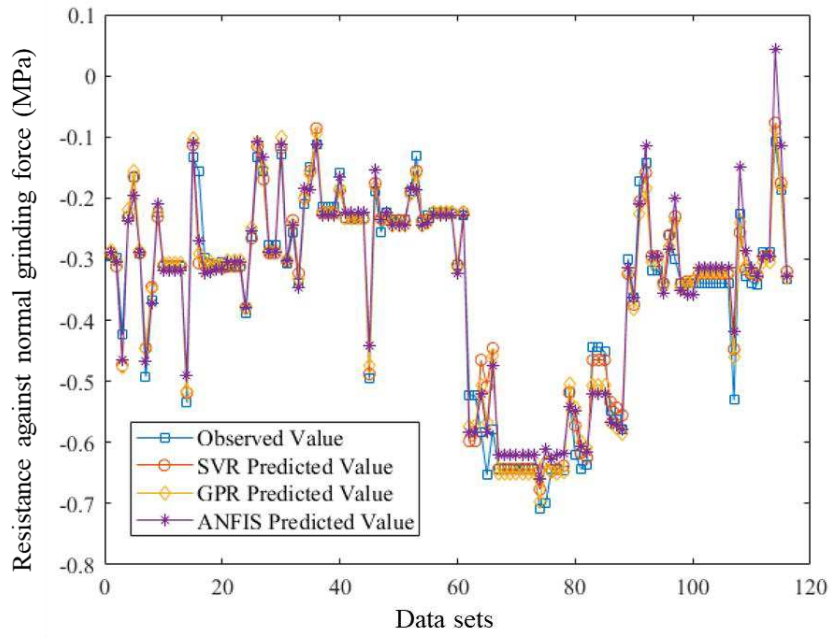


Fig 14. Results of different methods.

Model	Adjusted R ²	Root mean square error
Support vector regression	0.9580	0.0012
Gaussian processes regression	0.9713	0.0259
Adaptive neuro fuzzy inference system	0.9688	0.0020

The adjusted R² values of all algorithms were revealed to be greater than 0.95, indicating that the three trained surrogate models can appropriately interpret the simulation results. The comparison of the RMSE results revealed that the SVR model produced the smallest error, followed by the ANFIS model. Compared with the SVR and ANFIS models, the GPR model produced the largest RMSE. This could be due to the relationship between how GPR was predicted and the sample size, that is, the randomness of the dataset was positively correlated with the number of samples. As a result, with the sample size of the present study, the RMSE results of the GPR model was slightly inferior to those of the other two models. Fig. 12 reveals that the GPR model produced extreme prediction values at specific points. Overall, under the data conditions of the present study, the three prediction models all produced favorable prediction results, and the SVR model achieved the best performance.

5. Conclusion

In the present study, a machine learning-based regression model is established to predict the clamping resistance against normal grinding force during optical glass lens centering; with this model, continuous finite element analyses can be conducted in a more time- and computing-efficient manner. In total, 590 sets of clamping parameters are used as training and testing samples for three regression

algorithm models (i.e., SVR, GPR, and ANFIS). Among the three models, the SVR model has the most favorable performance with an adjusted R2 of 0.9580 and an RMSE of 0.0012. The applicability and robustness of the SVR model can be further enhanced through field verification and optimization algorithms.

6. Declaration

a. Funding

The authors are grateful for the support of the Research Project of the Ministry of Science and Technology, Taiwan (MOST 110-2222-E-007 -009 -MY3 & MOST 110-2218-E-007 -053).

b. Conflicts of interest/Competing interests

The authors declare no competing interests.

c. Availability of data and material

Not applicable.

d. Code availability

Not applicable.

e. Ethics approval

Not applicable.

f. Consent to participate

All authors were fully involved in the study and preparation of the manuscript; each of the authors has read and concurs with the content in the final manuscript.

g. Consent for publication

All authors consent to publish the content in the final manuscript.

h. Authors' contributions

Chun-Wei Liu: Conceptualization, Supervision,

Shaiu-Cheng Shiu: Finite Element Simulation, Convergence Analysis

Kai-Hung Yu: Experiment Design, Writing, Algorithmic Modeling

7. References

[1] S. M. Latyev, D. M. Rumyantsev, P. A. Kuritsyn (2013) "Design and process methods of centering lens systems", *Journal of Optical Technology* 80(3): 197-200.

[2] M. Beier, A. Gebhardt, R. Eberhardt, A. Tünnermann, Lens Centering of Aspheres for High-quality Optics, THOSS Media & DE GRUYTER, *Advanced Optical Technology*, 1(6), 441-446 (2012).

[3] C.W. Liu, S. C. Shiu, K. H. Yu (2022) Analysis of the optical quartz lens centering process based on acoustic emission signal processing and the support vector machine, *The International Journal of Advanced Manufacturing Technology*.

[4] F. Dengkui, D. Wenfeng, M. Qing, X. Jiuhua (2017) Simulation research on the grinding forces and stresses distribution in single-grain surface grinding of Ti-6Al-4V alloy when considering the actual cutting-depth variation, *The International Journal of Advanced Manufacturing Technology* 91 (9-12)

[5] M. F. Javed, N. H. Ramli, S. Kashif-ur-Rehman, N. B. Khan (2017) Finite element analysis on the structural behaviour of square CFST beams, *IOP Conference Series Materials Science and Engineering*

- 210(1):012018, 5–6 April 2017, University of Malaya, Kuala Lumpur, Malaysia.
- [6] Q. Ma, Z. Lin, Z. Yu, Prediction of deformation behavior and microstructure evolution in heavy forging by FEM, *Int J Adv Manuf Technol* (2009) 40:253–260.
- [7] V. Tuominen (2011) Virtual clamping in automotive production line measurement, *Expert Systems with Applications* 38: 15065–15074.
- [8] A. Olshevskiy, H. I. Yang, C. W. Kim (2011) Finite element simulation of inelastic contact for arbitrarily shaped rough bodies, *ARCHIVE Proceedings of the Institution of Mechanical Engineers Part C Journal of Mechanical Engineering Science 1989-1996 (vols 203-210)* 226(3):595-606.
- [9] Z. Liu, R. Kang, H. Liu, Z. Dong, Y. Bao, S. Gao, X. Zhu, FEM-based optimization approach to machining strategy for thin-walled parts made of hard and brittle materials, *The International Journal of Advanced Manufacturing Technology* (2020) 110:1399–1413.
- [10] K. S. Lee, J. C. Lin, Design of the runner and gating system parameters for a multi-cavity injection mould using FEM and neural network, *Int J Adv Manuf Technol* (2006) 27: 1089–1096.
- [11] M. Ryser, F. M. Neuhauser, C. Hein, P. Hora, M. Bambach, Surrogate model-based inverse parameter estimation in deep drawing using automatic knowledge acquisition, *The International Journal of Advanced Manufacturing Technology* (2021) 117:997–1013.
- [12] A. Hürkamp, S. Gellrich, A. Dér, C. Herrmann, K. Dröder, S. Thiede, Machine learning and simulation-based surrogate modelling for improved process chain operation, *The International Journal of Advanced Manufacturing Technology* (2021) 117:2297–2307.
- [13] C. C. António, S. Rasheed, A displacement field approach based on FEM-ANN and experiments for identification of elastic properties of composites, *The International Journal of Advanced Manufacturing Technology* (2018) 95:4279–4291.
- [14] G. Tapia, S. Khairallah, M. Matthews, W. E. King, A. Elwany, Gaussian process-based surrogate modeling framework for process planning in laser powder-bed fusion additive manufacturing of 316L stainless steel, *Int J Adv Manuf Technol* (2018) 94:3591–3603.
- [15] Z. Jun, Z. Youqiang, C. Wei, C. Fu, Research on prediction of contact stress of acetabular lining based on principal component analysis and support vector regression (2021) *Biotechnology & Biotechnological Equipment* 35 (1) 462-468.
- [16] T. Huang, X. Song, M. Liu, The multi-objective non-probabilistic interval optimization of the loading paths for T-shape tube hydroforming, *Int J Adv Manuf Technol* (2018) 94:677–686.
- [17] Y. Fan, W. Lu, T. Miao, Y. An, J. Li, J. Luo, Optimal design of groundwater pollution monitoring network based on the SVR surrogate model under uncertainty, *Environmental Science and Pollution Research* 27 (2020): 24090–24102
- [18] H. Xiang, Y. Li, H. Liao, C. Li, An adaptive surrogate model based on support vector regression and its application to the optimization of railway wind barriers, *Struct Multidisc Optim* (2017) 55:701–713.
- [19] Y. Liu, W. Chen, L. Ding, X. Wang, Response surface methodology based on support vector regression for polygon blank shape optimization design, *Int J Adv Manuf Technol* (2013) 66:1397–1405.

- [20] V. Rafiee, J. Faiz (2019) Robust Design of an Outer Rotor Permanent Magnet Motor Through Six-Sigma Methodology Using Response Surface Surrogate Model, IEEE TRANSACTIONS ON MAGNETICS 55 (10).
- [21] H. Naceur, S. Ben-Elechi, J. L. Batoz, C. Knopf-Lenoir (2008) Response surface methodology for the rapid design of aluminium sheet metal forming parameters, Materials & Design 29 (4): 781-790.
- [22] P. Jiang, L. Cao, Q. Zhou, Z. Gao, Y. Rong, X. Shao, Optimization of welding process parameters by combining Kriging surrogate with particle swarm optimization algorithm, Int J Adv Manuf Technol (2016) 86:2473–2483.
- [23] X. Ma, Z. Zhang, H. Hua (2022) Uncertainty quantization and reliability analysis for rotor/stator rub-impact using advanced Kriging surrogate model, Journal of Sound and Vibration 525 (12): 116800
- [24] K. Salonitis, A. Kolios, Reliability assessment of cutting tool life based on surrogate approximation methods, Int J Adv Manuf Technol (2014) 71:1197–1208.
- [25] L. F. Santos, C. B. B. Costa, J. A. Caballero, M. A. S. S. Ravagnani (2022) Framework for embedding black-box simulation into mathematical programming via kriging surrogate model applied to natural gas liquefaction process optimization, Applied Energy 310 (15) 118537.
- [26] B. Mohajernia, S. E. Mirazimzadeh, A. Pasha, R. J. Urbanic, Machine learning approaches for predicting geometric and mechanical characteristics for single P420 laser beads clad onto an AISI 1018 substrate, The International Journal of Advanced Manufacturing Technology (2022) 118:3691–3710.
- [27] I.D. Marinescu, W.B. Rowe, B. Dimitrov, I. Inasaki. (2004) TRIBOLOGY OF ABRASIVE MACHINING PROCESSES. Norwich, NY: William Andrew, Inc.
- [28] M. Gostimirović, D. Rodić, P. Kovač, D. Jesić, N. Kulundžić, (2015) Investigation of the cutting forces in creep-feed surface grinding process, Journal of Production Engineering 18 (2)
- [29] J. Lu, Z. Zhang, X. Yuan, J. Ma, S. Hu, B. Xue, X. Liao (2020), Effect of machining parameters on surface roughness for compacted graphite cast iron by analyzing covariance function of Gaussian process regression, Measurement 157 107578.
- [30] E. Jajarmi, S. A. Sajjadi, J. Mohebbi, Predicting the relative density and hardness of 3YPSZ/316L composites using adaptive neuro-fuzzy inference system and support vector, Measurement 145 (2019) 472–479.
- [31] M. Hourmand, A. A. D. Sarhan, S. Farahany, M. Sayuti, Microstructure characterization and maximization of the material removal rate in nano-powder mixed EDM of Al-Mg₂Si metal matrix composite—ANFIS and RSM approaches, The International Journal of Advanced Manufacturing Technology (2019) 101:2723–2737.